



PAPER

3D model-based super-resolution motion-corrected cardiac T1 mapping

OPEN ACCESS

RECEIVED
25 July 2022REVISED
26 September 2022ACCEPTED FOR PUBLICATION
20 October 2022PUBLISHED
9 December 2022

Original content from this work may be used under the terms of the [Creative Commons Attribution 4.0 licence](#).

Any further distribution of this work must maintain attribution to the author(s) and the title of the work, journal citation and DOI.



Simone Hufnagel^{1,*}, Selma Metzner¹, Kirsten Miriam Kerkering¹, Christoph Stefan Aigner¹, Andreas Kofler¹, Jeanette Schulz-Menger^{2,3,4}, Tobias Schaeffter^{1,5,6} and Christoph Kolbitsch¹

¹ Physikalisch-Technische Bundesanstalt (PTB), Braunschweig and Berlin, Germany

² Charité Medical Faculty University Medicine, Berlin, Germany

³ Working Group on Cardiovascular Magnetic Resonance, Experimental and Clinical Research Center (ECRC), Charité Humboldt University Berlin, DZHK partner site Berlin, Berlin, Germany

⁴ Department of Cardiology and Nephrology, HELIOS Klinikum Berlin Buch, Berlin, Germany

⁵ School of Biomedical Engineering and Imaging Sciences, King's College London, London, United Kingdom

⁶ Department of Biomedical Engineering, Technical University of Berlin, Berlin, Germany

* Author to whom any correspondence should be addressed.

E-mail: simone.hufnagel@ptb.de

Keywords: super-resolution, T1 mapping, model-based reconstruction, cardiovascular MR, myocardial tissue characterization

Supplementary material for this article is available [online](#)

Abstract

Objective. To provide 3D high-resolution cardiac T1 maps using model-based super-resolution reconstruction (SRR). **Approach.** Due to signal-to-noise ratio limitations and the motion of the heart during imaging, often 2D T1 maps with only low through-plane resolution (i.e. slice thickness of 6–8 mm) can be obtained. Here, a model-based SRR approach is presented, which combines multiple stacks of 2D acquisitions with 6–8 mm slice thickness and generates 3D high-resolution T1 maps with a slice thickness of 1.5–2 mm. Every stack was acquired in a different breath hold (BH) and any misalignment between BH was corrected retrospectively. The novelty of the proposed approach is the BH correction and the application of model-based SRR on cardiac T1 Mapping. The proposed approach was evaluated in numerical simulations and phantom experiments and demonstrated in four healthy subjects. **Main results.** Alignment of BH states was essential for SRR even in healthy volunteers. In simulations, respiratory motion could be estimated with an RMS error of 0.18 ± 0.28 mm. SRR improved the visualization of small structures. High accuracy and precision (average standard deviation of 69.62 ms) of the T1 values was ensured by SRR while the detectability of small structures increased by 40%. **Significance.** The proposed SRR approach provided T1 maps with high in-plane and high through-plane resolution ($1.3 \times 1.3 \times 1.5\text{--}2$ mm³). The approach led to improvements in the visualization of small structures and precise T1 values.

Introduction

Cardiovascular MR is a well-established technique for the diagnosis of cardiac diseases. Over the last years, T1 mapping has been translated into clinical application as an important quantitative approach for cardiac tissue differentiation (Guo *et al* 2022). It has been demonstrated that T1 mapping can be used to diagnose a wide range of different cardiac pathologies, including entities with preserved ejection fraction (Haaf *et al* 2016, Schelbert and Messroghli 2016, Al-Wakeel-Marquard *et al* 2021).

However, one of the major challenges in cardiac T1 mapping is that the achievable image resolution is often restricted due to respiratory and cardiac motion, signal-to-noise ratio (SNR) and limited acquisition time. In clinical practice, T1 maps are acquired with a 2D acquisition scheme resulting in one slice per breath hold (BH) that has a high in-plane but a poor through-plane resolution of 6–8 mm (Becker *et al* 2019). 3D T1 Mapping has been proposed but with a long acquisition time (Qi *et al* 2019, 2020). With the work proposed in Becker *et al*

(2020), 80% of the cardiac cycle can be used for T1 mapping, allowing the acquisition of six slices with a slice thickness of 6–8 mm per BH. Nonetheless, image resolution is compromised by partial volume effects. This can impair the accurate detection of subtle fibrosis in the myocardium in different entities and limit the capability to differentiate myocardial injury within the thin myocardial wall of young patients.

Super-resolution reconstruction (SRR) has been proposed to improve the tradeoff between spatial resolution, acquisition time and SNR (Greenspan *et al* 2002, Shuzhou *et al* 2006, Gholipour *et al* 2010, Kuklisova-Murgasova *et al* 2012, Plenge *et al* 2012, Kainz *et al* 2015, McDonagh *et al* 2017, de Senneville *et al* 2020, Ebner *et al* 2020, Sui *et al* 2019, 2021). The resolution is thereby increased by acquiring various low-resolution (LR) images with complementary information about the object. This is ensured by shifting the image positions of the LR stacks along the slice direction or by changing their slice orientations. Subsequently, the LR stacks are combined into a high-resolution (HR) dataset by solving an inverse problem. The reconstructed HR image thus benefits from the high SNR of the LR images while providing HR diagnostic information. For quantitative MRI, the parametric model of the mapping can be combined with the SRR model which has been demonstrated on the brain (Van Steenkiste *et al* 2017, Bano *et al* 2020). Such a model-based SRR enables the direct estimation of HR T1 maps from LR T1-weighted images (dynamics).

The principle of SRR is based on knowledge about the geometric relationship between different LR datasets. Motion leads to misalignment and strongly impairs the achievable image quality of SRR (Van Reeth *et al* 2012). The application of SRR on the heart (Rahman and Wesarg 2010a, 2010b, Dzyubachyk *et al* 2013, Shi *et al* 2013, Bhatia *et al* 2014, Odille *et al* 2015, Bastay and Grau 2018, Corona *et al* 2021, Xia *et al* 2021) has so far only been shown for qualitative imaging. For T1 Mapping, SRR taking into account different motion states of the individual LR stacks has so far only been applied on the brain (Van Steenkiste *et al* 2017, Beirinckx *et al* 2020, 2022).

The application of SRR to quantitative cardiac MRI data is especially challenging due to cardiac and respiratory motion. Next to that, the acquisition during BH imposes severe limitations on the acquisition time and thus limits the number of slices per LR stack. So far, no model-based SRR T1 mapping has been applied on cardiac data, which requires advanced acquisition and motion correction (moco) schemes.

In this study, we present a model-based SRR for cardiac T1 mapping, providing precise HR T1 maps with improved visualization of small structures compared to the direct LR acquisitions. It combined multiple stacks of 2D acquisitions with 6 to 8 mm slice thickness and generated 3D HR T1 maps with a target slice thickness of 1.5–2 mm in six to ten BH. Cardiac and residual respiratory motion was corrected. The approach was evaluated in native T1 mapping in numerical simulations and phantom experiments and feasibility was demonstrated in four healthy volunteers.

Methods

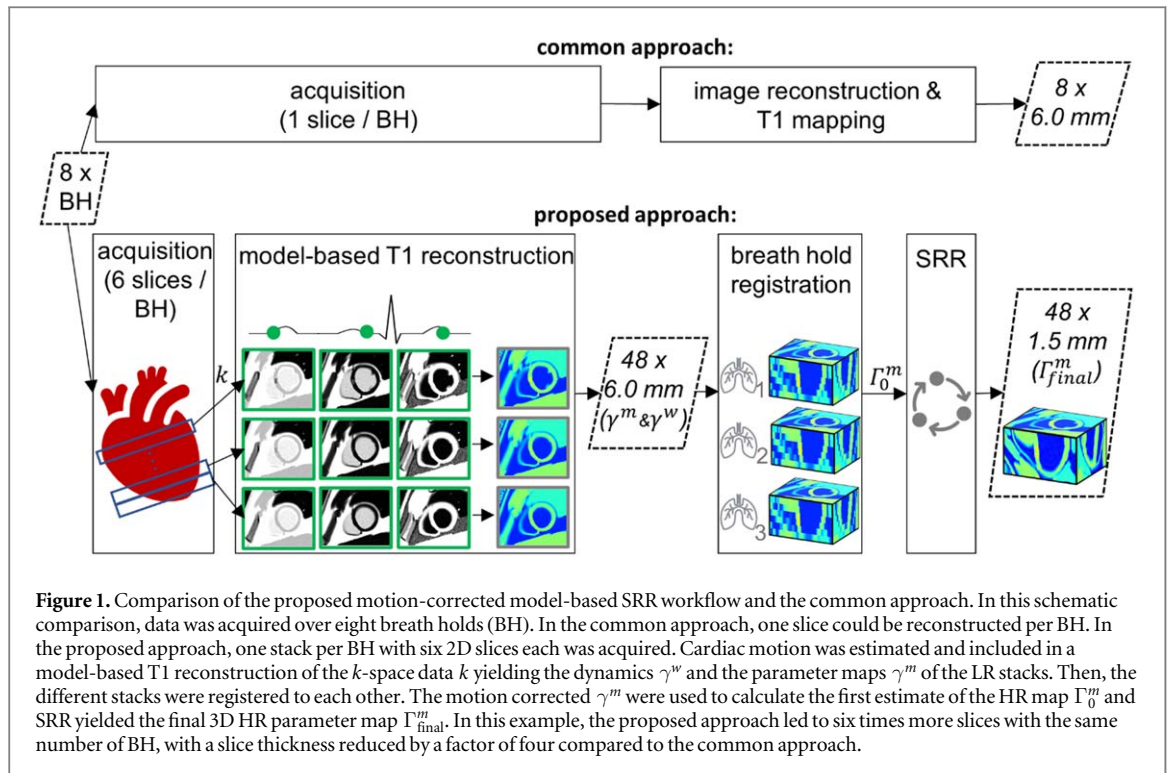
The proposed workflow to achieve motion-corrected model-based SRR T1 maps is depicted in figure 1: multiple stacks of 2D slices were acquired continuously with one stack per BH. In a first step, non-rigid cardiac motion was estimated and used in a model-based T1 reconstruction (Becker *et al* 2019) resulting in the dynamics γ^m and parameter maps γ^m (6 slices à 6–8 mm per stack) which were all in the same cardiac motion state. In a second step, the stacks were registered to each other to estimate and compensate for different BH positions. After the motion alignment, the maps were then used to calculate the first estimate of the HR map Γ_0^m as initialization of the SRR. Finally, a HR T1 map Γ_{final}^m was generated by SRR.

Data acquisition

Data was acquired using a Golden-angle radial sampling scheme on 3 Tesla MR scanner (Verio, Siemens Healthineers, Erlangen, Germany) with a commercial 32-channel cardiac coil. After a slice-selective radio-frequency inversion pulse, data was continuously acquired in multiple stacks with six slices each resulting in an acquisition time of 16.8 s for a single stack (2.8 s for each slice) with the following parameters: flip angle $\alpha = 5^\circ$, resolution $1.3 \times 1.3 \times 6.0\text{--}8.0 \text{ mm}^3$, field of view (FOV) $320 \times 320 \times 84\text{--}105 \text{ mm}^3$, TE/TR: 2.19/4.9 ms, orientation short-axis-view, subject specific slice gap of 4–9 mm to cover the desired FOV while avoiding slice interference from the radio-frequency inversion and excitation radio-frequency pulses. Six to ten stacks (one stack per BH) were acquired in total with an offset of 1.5–2 mm between stacks along the slice direction. Due to the short acquisition time, a slice-selective inversion pulse was used in combination with an interleaved multi-slice ordering. The ECG was recorded for retrospective cardiac moco.

Model-based T1 reconstruction

Dynamic cardiac motion-resolved images were reconstructed with a temporal resolution of 44.1 ms. Spatial and temporal total variation regularization (regularization parameters λ along time and space were 0.5) was applied



to suppress undersampling artefacts (Block *et al* 2007). To accelerate the motion estimation, a subject specific rectangular region of interest covering both ventricles was selected. In an iterative fashion, the non-rigid cardiac motion was estimated using the MIRTk Toolkit (Rueckert *et al* 1999).

The estimated cardiac motion information was used in an iterative model-based T1 reconstruction (Becker *et al* 2019, 2020). Data from the entire cardiac cycle was used, except for the 30% of the systole with the greatest through-plane motion. A Look-Locker model q was used in an iterative reconstruction scheme to estimate γ^m with the quantitative parameter $m = [p, \alpha, T1]$ and γ^w with a temporal resolution of 83.3 ms, p denoting the equilibrium magnetization and α the flip angle. In the following, only the T1 parameter is mainly considered because it is clinically the most relevant.

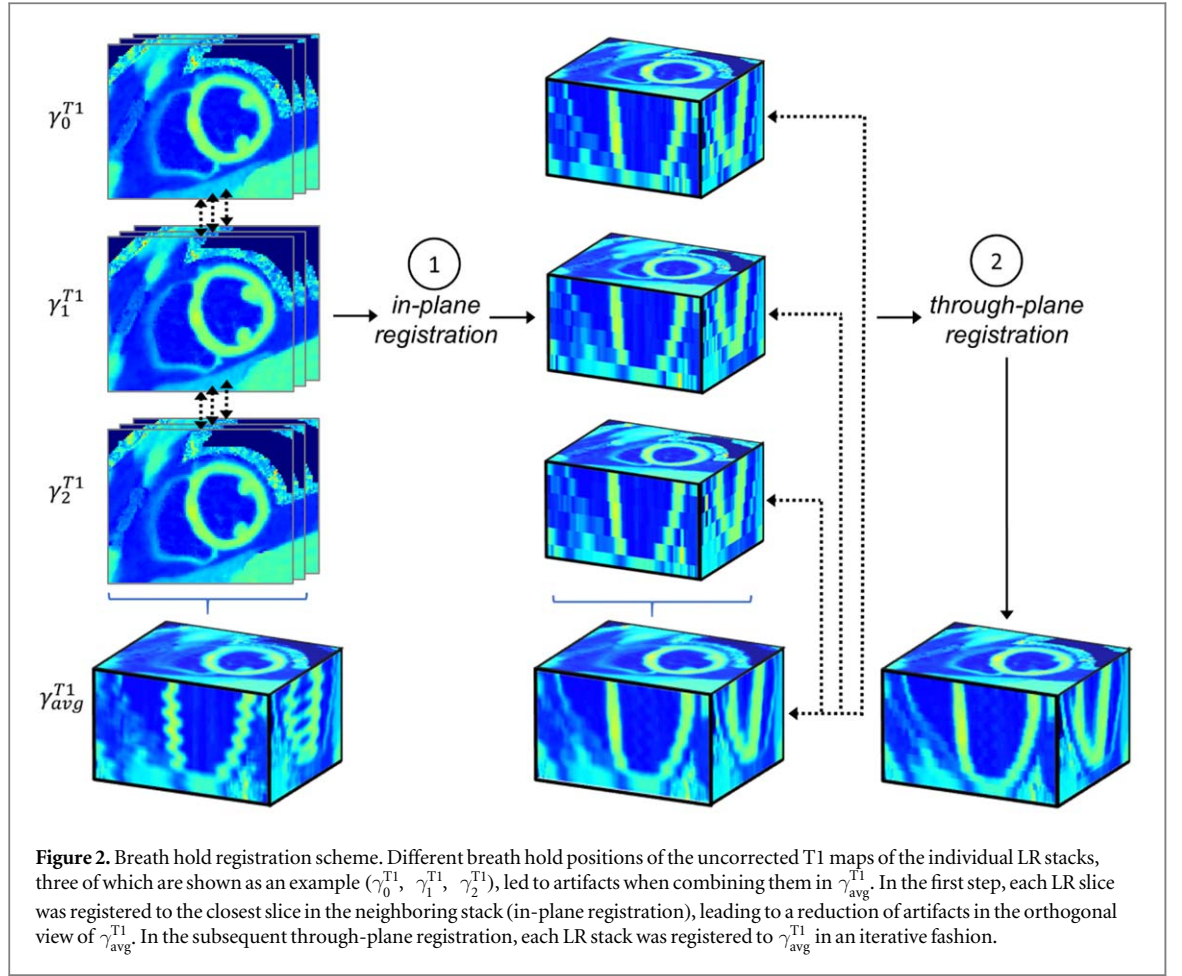
BH registration

Each stack was acquired in a different BH. To correct for potential misalignments of BH positions, the stacks were registered to each other using a cross-correlation approach (Padfield 2012). A two-stage process was developed for this purpose (figure 2). In the first step of the motion estimation, the rigid motion in the in-plane direction of the slices γ_s^m was determined. For that, the T1 maps of the LR slices of stacks s were registered to each other: each slice of each stack was registered to the slice which was closest (i.e. smallest distance along the slice direction) to it. The stacks were acquired in an overlapping fashion, therefore the closest slice was part of another stack and hence, γ_s^{T1} was registered to $\gamma_{(s-1)}^{T1}$ using a phase-cross-correlation registration. That yielded information about the in-plane motion of every slice of every stack. The median of the motion detected in its six slices was finally assigned to the entire stack of LR slices.

In the second step, the LR stacks were registered with respect to shifts along the slice encoding direction. For that, γ_s^{T1} was interpolated along the slice encoding direction using bicubic spline interpolation, which also filled the gaps between the LR slices. The interpolated T1 maps of the LR stacks were then combined and an average stack γ_{avg}^{T1} was calculated. In an iterative process, each stack was then registered to γ_{avg}^{T1} . In the next iteration a new γ_{avg}^{T1} was calculated taking the estimated motion into account. Only translational shifts were considered. Two iterations were used in total.

Model-based SRR

For SRR, several LR stacks acquired with an offset to each other were combined to a HR volume. The model q calculates dynamics from given parameter maps. The SRR used here is model-based and thus q was incorporated into SRR to at the end obtain a HR T1 map Γ_0^m from γ^w . As initialization Γ_0^m of the SRR, γ^m were calculated from γ^w using a voxel-wise three-parameter T1 fit and combined:



$$\Gamma_{0,h}^m = \sum_{s=1}^S \sum_{l=1}^L a_s^{h,l} \gamma_{s,l}^m \quad (1)$$

In order to describe the effect of the excitation slice profile, a resolution model was calculated from Bloch simulations of the RF pulse (Pauly *et al* 1991, Rund *et al* 2018). The slice profile simulations were used to describe the weight $a_s^{h,l}$ of HR slice h with respect to LR slice l in stack s (with $h = 1, \dots, H$, $l = 1, \dots, L$ and $s = 1, \dots, S$ and H , L , and S being the number of HR-slices, the number of LR-slices and the number of stacks, respectively). With that, LR dynamics $\tilde{\gamma}_{t,s,l}^w$ (with $t = 1, \dots, T$, and T being the number of inversion times) were calculated:

$$\tilde{\gamma}_{t,s,l}^w(\Gamma^m) = \sum_{h=1}^H a_s^{h,l} q_t(\Gamma_h^m) \quad (2)$$

A functional based on the sum of the differences between the LR slices and stacks of the predicted ($\tilde{\gamma}_{t,s,l}^w$) and acquired LR dynamics ($\gamma_{t,s,l}^w$) and a total variation based regularization term was minimized, which could be described by the following minimization problem:

$$\min_{\Gamma^m} \sum_{t=1}^T \sum_{s=1}^S \sum_{l=1}^L \|\gamma_{t,s,l}^w - \tilde{\gamma}_{t,s,l}^w(\Gamma^m)\|_2^2 + \kappa \|\mathbf{G}\Gamma^m\|_1 \quad (3)$$

where κ describes the regularization parameter and \mathbf{G} corresponds to the forward finite differences operator. As $a_s^{h,l}$ describes the relationship between a HR and LR slice, by solving problem (3) an estimate of the HR slices could be recovered. Since solving problem (3) directly is challenging due to the non-smoothness of the L1-norm as well as the non-linear function q , a variable splitting (Wang *et al* 2008, Bano *et al* 2020) approach was used. This allowed solving the resulting sub-problems with suitable algorithms. By introducing auxiliary variables $x_t := q_t(\Gamma^m)$ for all t and $u := \Gamma^m$ the problem was reformulated as a joint minimization problem. These equalities were relaxed by including two quadratic penalty terms, weighted by λ and μ , yielding:

$$\begin{aligned} \min_{\Gamma^m, x, u} \sum_{t=1}^T \sum_{s=1}^S \sum_{l=1}^L \left\| \gamma_{t,s,l}^w - \sum_{h=1}^H a_s^{h,l} x_{t,h} \right\|_2^2 + \lambda \|x_t - q_t(\Gamma^m)\|_2^2 \\ + \mu \|u - \Gamma^m\|_2^2 + \kappa \|Gu\|_1. \end{aligned} \quad (4)$$

The solution of problem (4) was approached by alternating the minimization of (4) with respect to one of the variables and keeping the other two fixed. For fixed Γ^m , u , updating x corresponded to solving

$$\min_x \sum_{t=1}^T \sum_{s=1}^S \sum_{l=1}^L \left\| \gamma_{t,s,l}^w - \sum_{h=1}^H a_s^{h,l} x_{t,h} \right\|_2^2 + \lambda \|x_t - q_t(\Gamma^m)\|_2^2 \quad (4a)$$

Subproblem (4a) was minimized with respect to x , assuming Γ^m and u are fixed. Solving (4a) involved solving a linear system for which a conjugate gradient approach was used.

For fixed Γ^m , x , updating u in problem (4) corresponded to solving

$$\min_u \mu/\kappa \|u - \Gamma^m\|_2^2 + \|Gu\|_1. \quad (4b)$$

Subproblem (4b) was solved using the iterative algorithm proposed in Chambolle (2004).

For fixed u and x , updating Γ^m in problem (4) corresponded to solving

$$\min_{\Gamma^m} \sum_{t=1}^T \lambda \|x_t - q_t(\Gamma^m)\|_2^2 + \mu \|u - \Gamma^m\|_2^2. \quad (4c)$$

Due to the non-linearity of function q , the Limited-memory Broyden–Fletcher–Goldfarb–Shanno algorithm (Liu and Nocedal 1989) was used for solving problem (4c). To solve problem (4), the subproblems were alternated eight times and the solution of problem (3) was referred to as Γ_{final}^m .

Simulation experiments

Simulated data was generated using the XCAT phantom (Segars *et al* 2010). A dataset X_{orig} with the voxel size $1.3 \times 1.3 \times 0.5$ mm was generated. From this, eight stacks of LR dynamics were simulated with the same parameters used for the phantom and the *in vivo* experiments (slice thickness of 6 mm, a gap between the LR slices of 6 mm and an offset between the stacks of 1.5 mm). As reference X_{ref} , a dataset with a slice thickness of 1.5 mm was generated from X_{orig} . In X_{orig} , two cubical fibrotic structures were simulated in the septum with a width of 6 mm each along the slice encoding direction. They were separated by a 6 mm gap of healthy myocardium. Cardiac motion was simulated using the default settings of the XCAT phantom. Data acquisition was simulated with multiple receiver coils using the same acquisition parameters as for the phantom and the *in vivo* experiments. Zero-mean noise was added. This allowed the application of the entire pipeline including model-based T1 reconstruction and cardiac moco on the simulated data.

In the simulations, a T1 time of 1300 ms was assigned to the myocardium, 400 ms to fat, 800 ms to the liver, 900 ms to muscle and 1800 ms to the simulated fibrosis. Blood was simulated with an apparent T1 time of 350 ms, as it could not be estimated due to the in-flow effect caused by the slice-selective inversion pulse (Keith *et al* 2017).

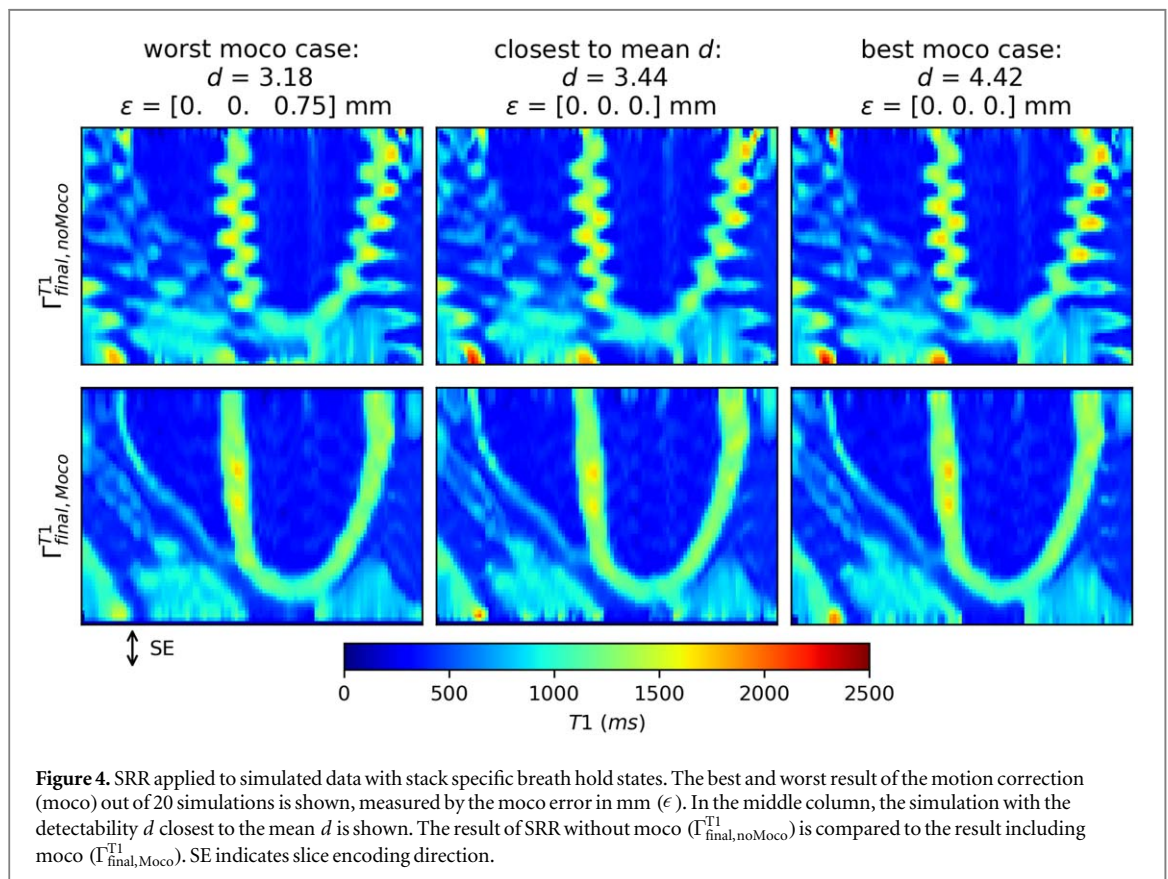
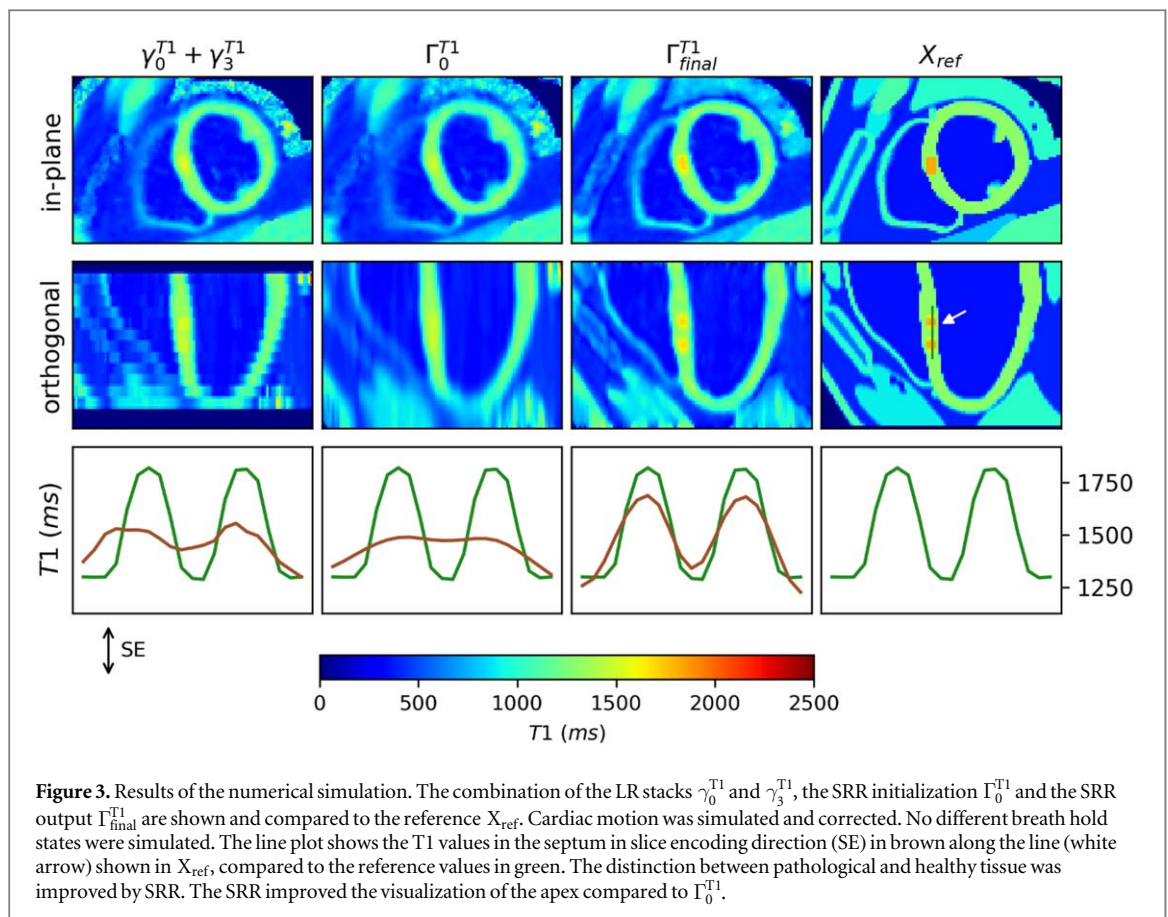
Two different types of simulations were carried out. First, a simulation assuming perfect BH (i.e. no misalignment between different BH) was performed to evaluate the possible improvement that could be achieved with SRR. In a second step, misalignment between the BH was included into the simulation. Different BH positions were simulated by applying translation shifts. 20 configurations with different breath-hold positions of the stacks were simulated. The simulated motion was in the range of (3.5, 1.9, 8.2) mm in the (anterior–posterior, right–left, food–head) direction, based on half of the motion range between end expiration and end inspiration measured in (Scott *et al* 2009). For reasons of computational time, no heart motion was included in this simulation.

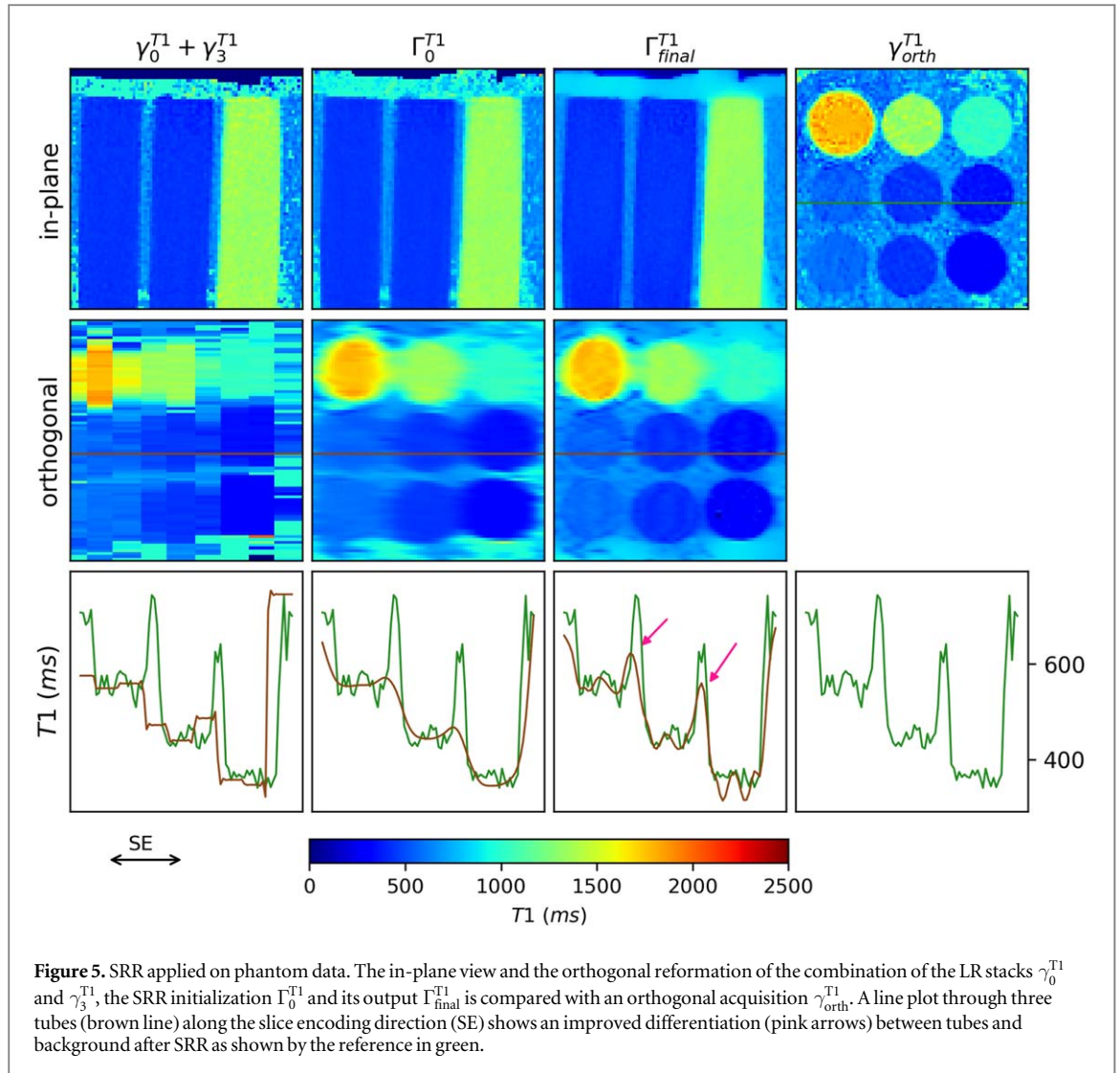
To assess the outcome of the SRR applied on simulated data, the detectability d between the simulated fibrosis and surrounding healthy myocardium was measured, using the following formula:

$$d = (\mu_{\text{structure}} - \mu_{\text{nextStructure}}) / \sigma_{\text{background}}, \quad (5)$$

where the mean T1 value $\mu_{\text{structure}}$ was measured in a region-of-interest (ROI) within the fibrosis, the mean T1 value $\mu_{\text{nextStructure}}$ was calculated in a ROI next to the fibrosis and the standard deviation (SD) $\sigma_{\text{background}}$ was calculated from a ROI in the surrounding healthy myocardium. The ROI was calculated from the position of the simulated fibrotic structures in X_{orig} .

To evaluate the breathing moco, the RMS error $\in \epsilon$ between the originally simulated motion and the estimated motion was calculated in mm.





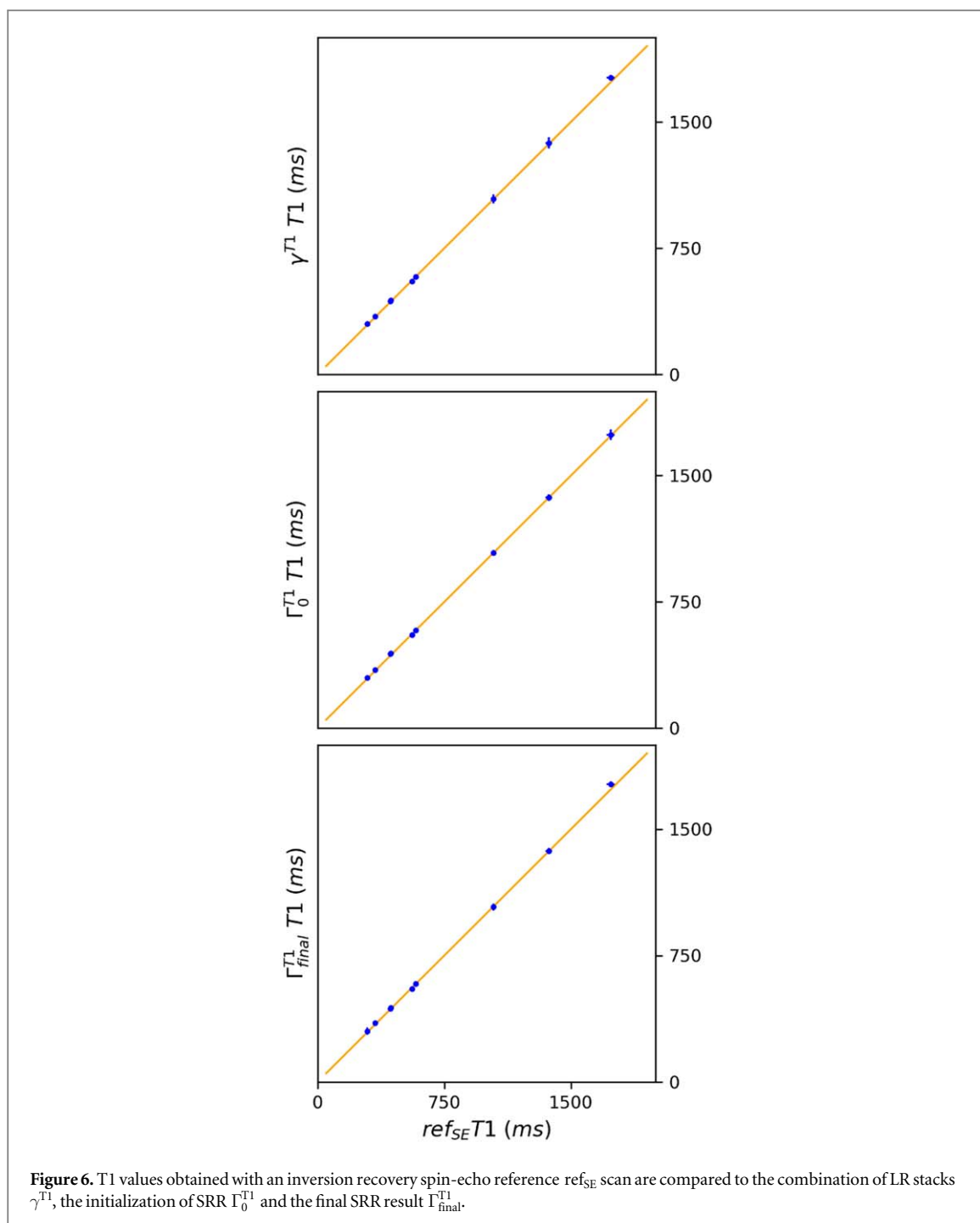
The LR data in the proposed approach was always acquired in the same orientation according to the short-axis-view of the heart. To assess through-plane resolution, images in this publication are often presented orthogonally from the side, resulting in a four-chamber view.

Phantom experiments

To evaluate the proposed approach in phantom measurements, imaging was performed with the above-described scan parameter in a ‘T1MES-phantom’ with nine tubes with different T1 times developed for cardiac imaging (Captur *et al* 2016). In order to cover the whole phantom with every stack, 12 slices per stack were acquired. Furthermore, a scan γ_{orth}^m orthogonal to the LR data was acquired, where the slice encoding direction of γ^m became an in-plane direction of γ_{orth}^m . As a reference, an inversion recovery spin-echo ref_{SE} was acquired, also in orthogonal direction to the LR data with 7 TIs between 25 and 4800 ms (TE/TR: 12/8000 ms, FOV: $143 \times 160 \text{ mm}^2$, spatial resolution: $0.8 \times 0.8 \times 5 \text{ mm}^3$).

To assess the outcome of the SRR applied on the T1MES phantom, a ROI was drawn in every tube in γ^m , Γ_0^m , Γ_{final}^m and ref_{SE} . The mean and SD of the T1 values were compared to assess T1 accuracy and precision, respectively. The Pearson’s correlation coefficient and the two-tailed *P*-value between γ^m , Γ_0^m , Γ_{final}^m and ref_{SE} were calculated.

To evaluate the outcome of the BH moco, another dataset was acquired with phantom data at different, well-defined positions simulating different BH positions. The different positions were in the range (5.0, 2.4, 5.0) mm compared to the reference position. The reference motion was known for this acquisition and the root-mean-squared error (RMSE) to the estimated motion was calculated.



***In vivo* experiments**

To evaluate the proposed approach in *in vivo* measurements, data was obtained from four healthy subjects (4 males, aged 34.0 ± 11.7 y). All subjects gave written informed consent before participation, in accordance with the institution's ethical committee. For the *in vivo* data, an orthogonal scan γ_{orth}^m was acquired.

For reference, a 3(3)3(3)5 modified Look–Locker inversion recovery (MOLLI) scan Γ^{MOLLI} was acquired with the following scan parameter: FOV: 360×306 mm², TE/TR: 1.12/2.7 ms, flip angle: 35°, and spatial resolution: $2.1 \times 1.4 \times 6$ mm³ once in four chamber (4CH) and once in two chamber (2CH) orientation. The T1 values of the SRR result and MOLLI reference were compared using a ROI placed in the septum.

To assess the outcome of the SRR applied on *in vivo* data, γ_{orth}^m was qualitatively compared to Γ_{final}^m . The precision of the T1 values was evaluated quantitatively by comparing the bull's eye plots (Weissman *et al* 2002) before and after the SRR, using four selected slices (apex, apical, mid-cavity and basal) and calculating the SD over four healthy volunteers. No fibrotic tissue was present in the healthy volunteers and therefore the detectability of the right ventricle was calculated to assess the effect of SRR on small structures.

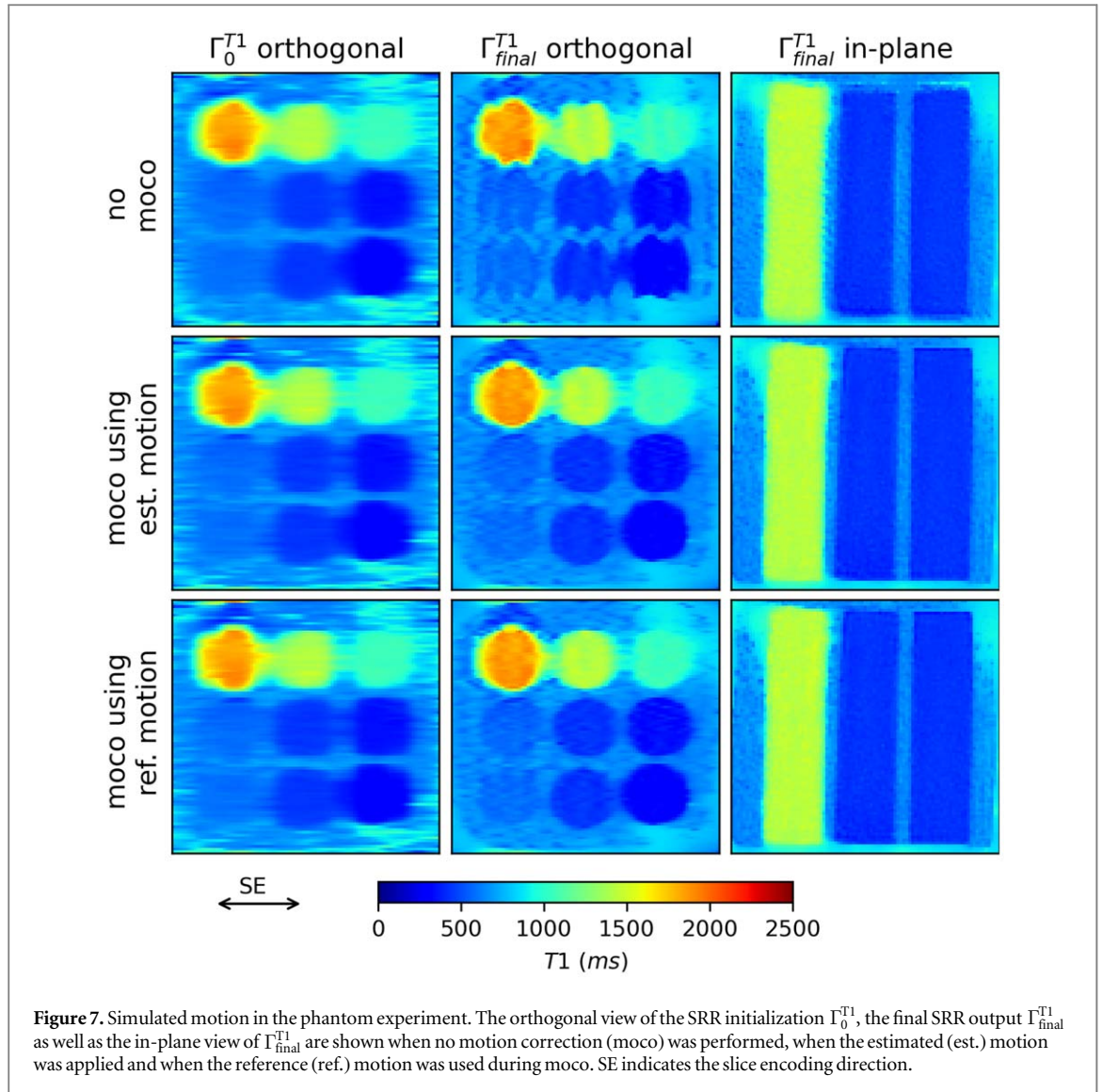


Figure 7. Simulated motion in the phantom experiment. The orthogonal view of the SRR initialization Γ_0^{T1} , the final SRR output $\Gamma_{\text{final}}^{\text{T1}}$ as well as the in-plane view of $\Gamma_{\text{final}}^{\text{T1}}$ are shown when no motion correction (moco) was performed, when the estimated (est.) motion was applied and when the reference (ref.) motion was used during moco. SE indicates the slice encoding direction.

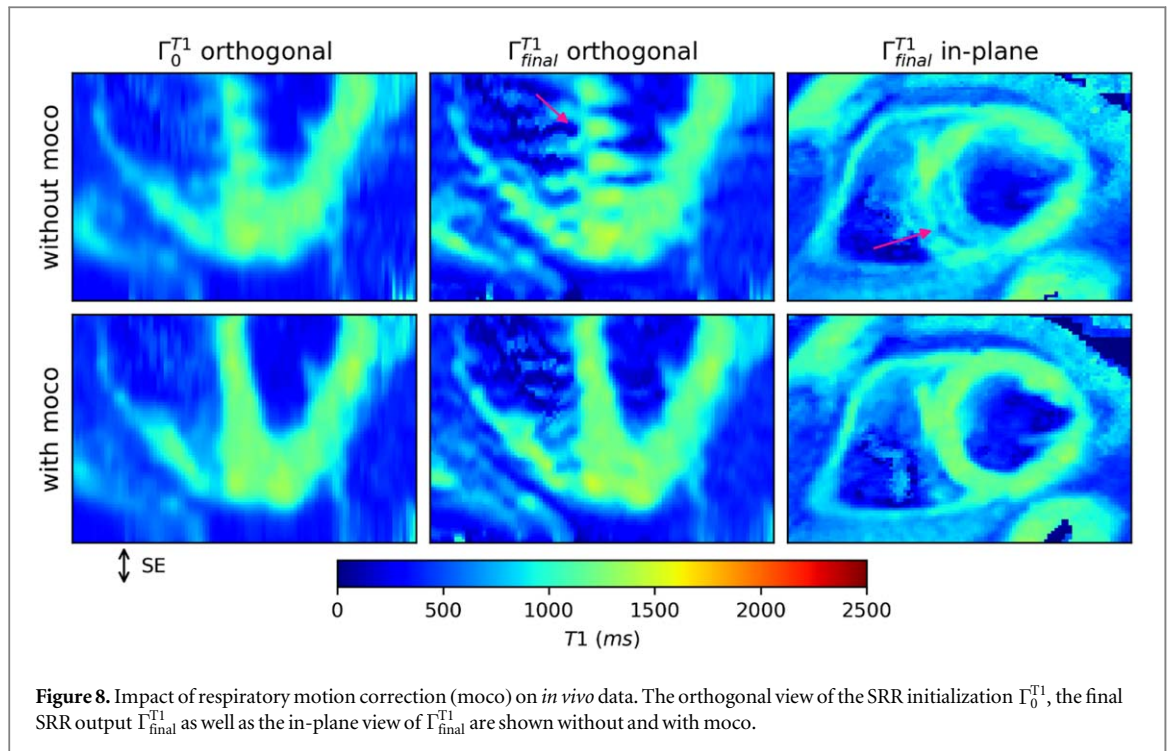
The edge sharpness of the left ventricle in the anterior apical segment of the ventricle was calculated for γ^m , Γ_0^m and Γ_{final}^m . Edge sharpness was calculated by manually drawing a line along the edge of interest, gathering the intensities perpendicular to the line, and generating an average edge profile. The first-order derivative of the edge profile was calculated and edge sharpness of 100% referred to the case when the maximum derivative of the average edge profile was equal to the maximum intensity difference in the average edge profile, similar to Etienne *et al* (2002).

Results

Simulation experiments

Figure 3 shows the results of the numerical simulations assuming perfect BH positions. In the LR stacks the two different fibrotic structures could not be distinguished along the slice encoding direction. The apex was inaccurately depicted in Γ_0^{T1} . Its visualization improved after SRR. d of the fibrosis increased from 0.03 in Γ_0^{T1} to 4.38 in $\Gamma_{\text{final}}^{\text{T1}}$.

Figure 4 shows the SRR applied on simulated data, simulated with different BH positions for every stack. $\Gamma_{\text{final}}^{\text{T1}}$ is shown without moco ($\Gamma_{\text{final, noMoco}}^{\text{T1}}$) and with applying the calculated motion ($\Gamma_{\text{final, Moco}}^{\text{T1}}$), once from the simulation with $\epsilon = 0$ (best case), with the largest ϵ (worst case) and once for the simulation with a d closest to the mean d of all simulations. Moco improved the outcome of the SRR. In the best moco case, the differentiation of healthy and pathological tissue was more clear compared to the worst moco case. d of the simulated fibrosis over all 20 simulations after applying the calculated motion was 3.55 ± 0.54 in $\Gamma_{\text{final, Moco}}^{\text{T1}}$. d after applying the correct motion was 3.62 ± 0.5 . d in $\Gamma_{\text{final, noMoco}}^{\text{T1}}$ was not calculated, because the fibrosis could not be detected for these T1 maps, as figure 4 shows. The error ϵ over all simulations was $(0.0, 0.0, 0.18) \pm (0.0, 0.0, 0.28)$ mm.



Phantom experiments

Figure 5 shows the in-plane view and the orthogonal reformation of γ^{T1} , Γ_0^{T1} and Γ_{final}^{T1} and compares it to an orthogonal acquisition γ_{orth}^{T1} . A line plot through three tubes along the slice encoding direction shows an improved differentiation between tubes and background after SRR.

Figure 6 assesses the accuracy of SRR: γ^{T1} , Γ_0^{T1} and Γ_{final}^{T1} showed high correlation with the reference scan ($P < 0.001$, $R^2 > 0.999$). The mean difference between the T1 values of ref_{SE} and Γ_{final}^{T1} was 7.65 ± 9.24 ms. The difference of γ^{T1} and Γ_0^{T1} to ref_{SE} was 7.74 ± 7.09 ms and 5.41 ± 3.7 ms, respectively, indicating high accuracy of the SRR.

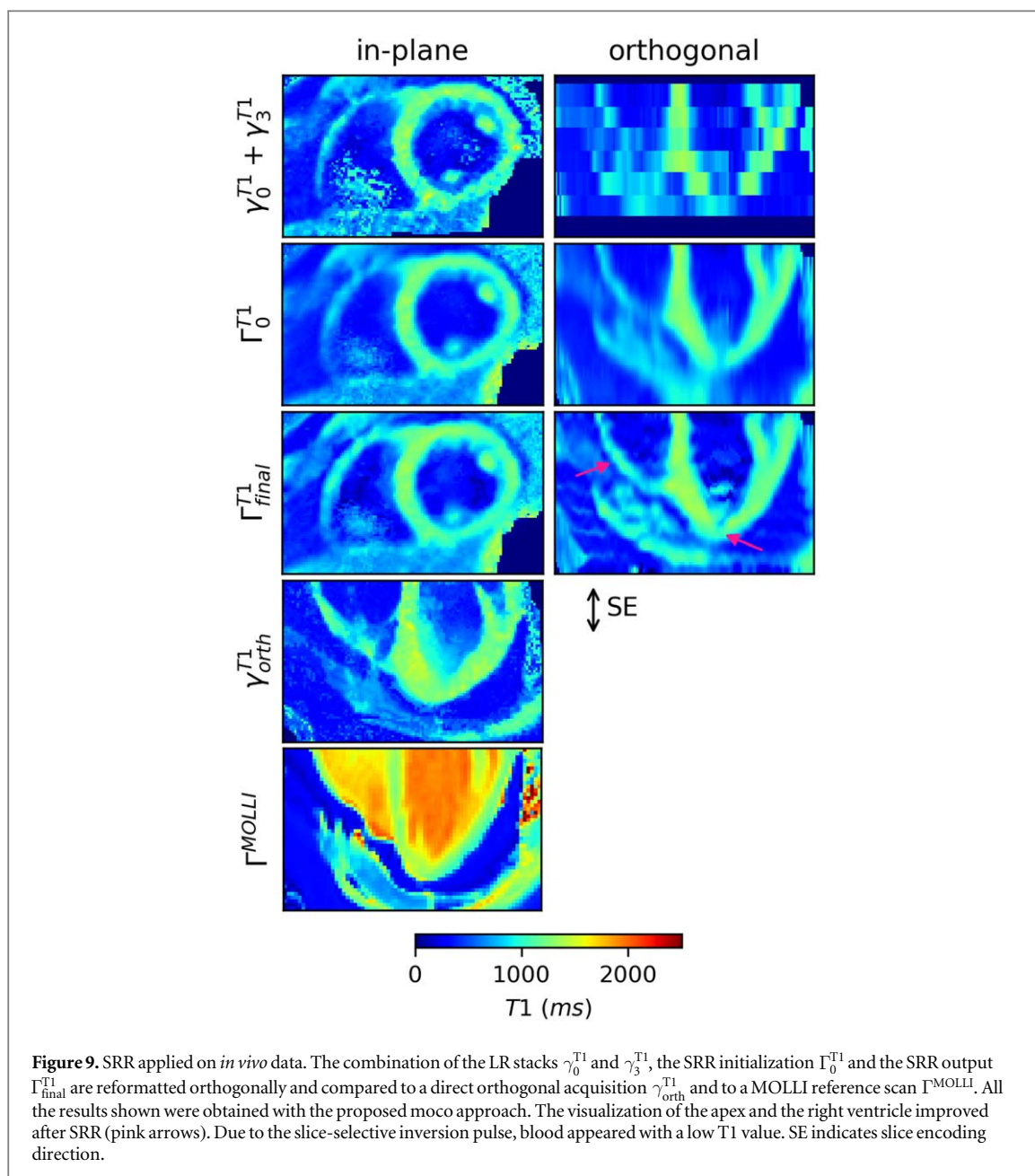
Figure 7 shows the application of SRR on phantom data acquired at different positions simulating different BH positions. The orthogonal view of Γ_0^{T1} and Γ_{final}^{T1} and the in-plane view of Γ_{final}^{T1} are shown without moco, when the estimated motion was applied and when the reference motion was applied during moco. SRR without moco shows motion artefacts, which could be removed after applying the calculated moco. The visual result after applying the estimated motion shifts is similar to applying the reference motion shifts during moco. The RMSE between estimated and reference motion was (0.03, 0.04, 0.61) mm.

In vivo experiments

Figure 8 compares the orthogonal view of Γ_0^{T1} and Γ_{final}^{T1} and the in-plane view of Γ_{final}^{T1} with and without moco. Without BH alignment, motion artefacts could be seen in the form of a discontinuous septum in the orthogonal view and an ambiguous delineation of the myocardium in the in-plane view, which is highlighted by the pink arrows in the figure. The motion artefacts were less visible in the initialization of the SRR compared to its output. Using the proposed BH registration and subsequent correction, the motion artefacts after SRR could be reduced.

Figure 9 shows the in-plane view and the orthogonal reformation of γ^{T1} , Γ_0^{T1} , Γ_{final}^{T1} and compares it to an orthogonal acquisition γ_{orth}^{T1} and Γ^{MOLLI} . Due to the slice-selective inversion pulse, blood appeared with a low T1 value. The visualization of the apex as well as the differentiation between the right ventricle and blood improved after SRR. Due to scan time limitations, γ_{orth}^{T1} could not be acquired for one volunteer. The mean T1 value across all volunteers in a ROI in the septum in Γ_{final}^{T1} was 1211.49 ± 75.17 ms and in Γ^{MOLLI} 1276.11 ± 38.77 ms. One volunteer had to be excluded from the calculation because no MOLLI scan was available.

In figure 10, four selected slices (apex, apical, mid-cavity and basal) of γ^{T1} , Γ_0^{T1} , Γ_{final}^{T1} are compared in-plane. The apex was more clearly visible in the apex slice after SRR. The visualization of the right ventricle also improved after SRR. In addition, the combination of multiple LR slices in the SRR also reduced artefacts (black arrow in figure 10) and improved e.g. the quantification of the inferolateral segment of the basal slice. d in the right ventricle increased from 2.4 ± 1.35 in γ^m , to 3.2 ± 1.63 in Γ_0^m and 3.35 ± 1.39 in Γ_{final}^{T1} , thus an increase of d by 40% from γ^m to Γ_{final}^{T1} . The edge sharpness in the anterior apical segment was 0.26 ± 0.04 in γ^m , 0.21 ± 0.02 in Γ_0^m and 0.26 ± 0.04 in Γ_{final}^{T1} . The sharpness of the ventricle was lower in the SRR

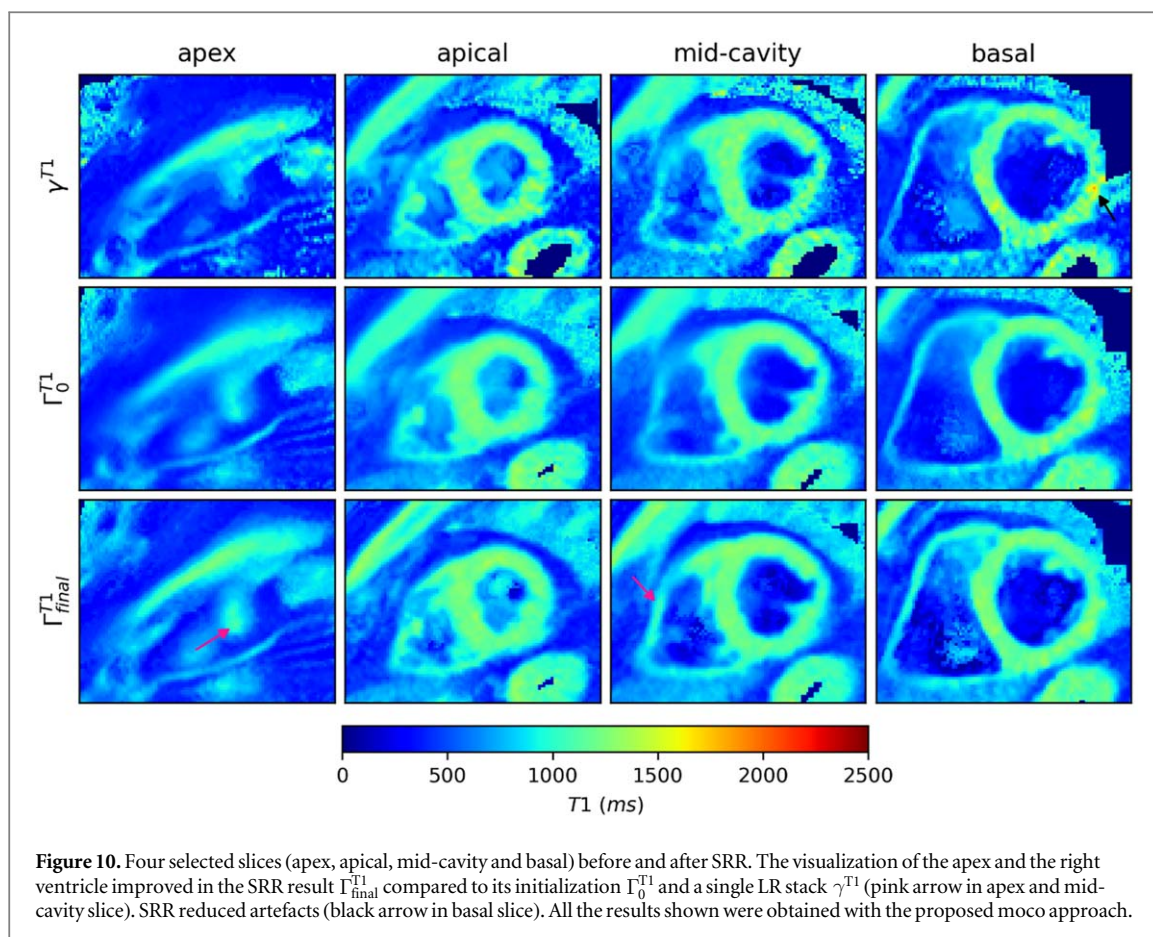


initialization than in the LR images, which could be attributed to the mixing of the partial volume effects in the individual LR images when combining them for the initialization. SRR was able to restore the original edge sharpness of the LR images. T1 maps of the three other volunteers can be seen in Supporting Information figure S1.

Figure 11 shows the bulls-eye plots of γ^{T1} , Γ_0^{T1} and Γ_{final}^{T1} , averaged over four healthy volunteers. The SD before and after the SRR remained comparable, indicating that SRR did not affect the precision of the T1 values. The T1 values in the segments varied in Γ_{final}^{T1} by an average of 63.72 ms across the four healthy volunteers. The T1 intensities of the apex segment were underestimated before the SRR and showed a high SD. This was compensated by SRR.

Discussion

In this study, a novel motion-corrected model-based SRR approach was presented, providing 3D HR T1 maps in six to ten 17 s BH. The proposed model-based SRR scheme improved the visibility of small structures while the accuracy and precision of the T1 values after SRR remained comparably high. An alignment of different BH states showed great improvement of the SRR result.



Small structures, as e.g. the simulated fibrosis, the differentiation between phantom tubes and background or the right ventricle could be better visualized using SRR. Furthermore, anatomic information which was impaired in some LR stacks due to partial volume effects, as e.g. the apex, was successfully recovered by the proposed SRR approach.

An improvement in the imaging of small features by SRR can be concluded from the improved visualization of small structures in all volunteers of the *in vivo* experiments, such as in the right ventricle.

The accurate mapping of the right ventricular myocardium poses a great challenge due to its small thickness but would help to improve the diagnosis of e.g. right ventricular myocarditis or arrhythmogenic right ventricular cardiomyopathy. Its assessment could be improved by SRR, moving towards whole heart T1 mapping in the future.

The results were compared to a clinical reference scan and the T1 values after SRR were in good agreement with both the reference values resulting from the modified Look–Locker inversion recovery reference scan and those presented in literature (von Knobelsdorff-Brenkenhoff *et al* 2013). The small underestimation of the myocardial T1 values after the SRR compared to reference values was probably due to the use of a slice-selective inversion pulse. A similar underestimation of the T1 values was reported in Huang *et al* (2020), which was attributed to magnetization transfer effects. A direct comparison of the SRR result to an *in vivo* reference scan was however difficult since this was acquired in another BH, hence showing a different motion state. Thus, the accuracy of the T1 values could only be determined in phantom measurement but not in the volunteer scans.

The proposed approach was not compared to previously published 3D T1 mapping frameworks as for example MR multitasking (Christodoulou *et al* 2018) or MR fingerprinting (Ma *et al* 2013). Nonetheless, the publications in this field have either not resulted in isotropic voxel sizes (Guo *et al* 2018, Cruz *et al* 2020, Ferreira da Silva *et al* 2020, Nordio *et al* 2017, 2020, Han *et al* 2022, Mao *et al* 2022, Velasco *et al* 2022) or a longer total scan time (Milotta *et al* 2020, Qi *et al* 2019, 2020) compared to the proposed approach.

The precision of the T1 values was not calculated with a retest but as the SD over several healthy volunteers. It was assumed, that the T1 values of the myocardium were similar in all healthy volunteers.

One limitation of this approach is that T1 values of voxels representing blood could not be estimated and appeared shortened, due to the in-flow effect caused by the slice-selective inversion pulse. The slice-selective inversion pulse only inverted the blood spins that were in the corresponding slice at the time of the inversion. In the course of the cardiac cycle, these were replaced by inflowing, non-inverted blood spins, which then lead to an

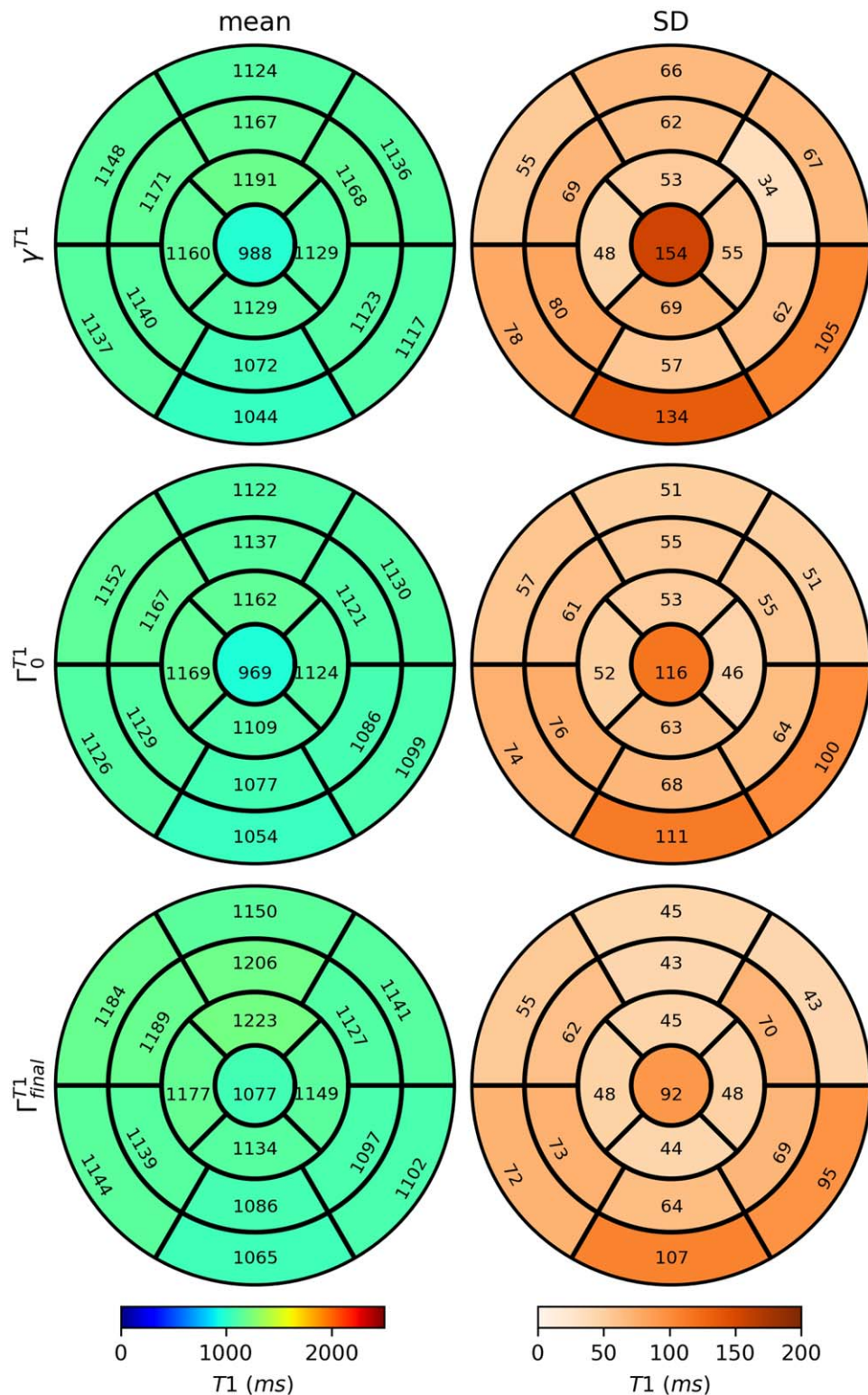


Figure 11. Bull's eye plots of the average T1 values in ms in standardized segments of the left ventricle and their standard deviation (SD). The SRR output Γ_{final}^{T1} is compared to a LR slice γ^{T1} and the SRR initialization Γ_0^{T1} .

apparent shortening of the T1 value of the blood (Keith et al 2017). To still be able to calculate the extracellular volume, a further fast acquisition of a single LR slice with a global inversion pulse would provide the necessary information about the blood pool T1 values.

Every stack was acquired in a separate BH. Due to variations in BH, an alignment of different BH states was necessary before SRR. In agreement with Van Reeth et al (2012), motion estimation was a key step in the SRR process and significantly affected the quality of the SRR result. Imperfectness in moco could lead to artefacts after SRR.

In clinical practice, 17 s BH are sometimes not feasible. To adapt the BH duration, the acquisition time per stack would need to be reduced and compensated for by acquiring more stacks in total. Due to the higher number of stacks, the proposed moco approach would have an even greater influence on the SRR result.

Compared to brain T1 mapping, cardiac imaging is restricted with respect to the number of LR slices per stack, due to limited BH time. To still cover a specific field-of-view in the slice encoding direction, gaps needed to be introduced between the LR slices. To compensate for these gaps, more stacks of LR slices needed to be acquired. According to Rahman and Wesarg (2010a), the more stacks used, the greater the degrading influence of inaccuracies in the motion registration on the SRR.

The stacks were planned such that they overlapped with each other by 1.5–2 mm. As each stack was obtained in a different BH position, the original distribution of stacks was impaired, even if the respiratory motion was correctly detected and estimated. Overall, the detectability of the simulated fibrosis was high in most of the motion corrected SRR maps. Nevertheless, depending on the distribution of stacks relative to each other after moco, the depiction of the fibrosis could still be impaired. This effect could in future be reduced by orientating the LR stacks differently (e.g. rotated to each other) along the slice encoding direction, which has also previously shown to improve SRR reconstructions compared to shifting the LR stacks (Shilling *et al* 2009).

The results of the moco could be improved by its integration into the optimization scheme of the SRR, as described in Dzyubachyk *et al* (2015). Furthermore, integrating rotation and deformation into the moco would probably further improve the alignment of BH states. Next to that, registering the slices within one stack separately to the HR volume would also account for inter stack motion due to poor breath holding. In addition, instead of retrospective BH correction, the position of the slices could be tracked prospectively and the acquisition adjusted accordingly, for example using the Pilot tone (Ludwig *et al* 2021). Next to that, SRR is not limited to T1 mapping, but could be extended to other quantitative parameters such as T2 (Giri *et al* 2009), for example using MR multitasking (Christodoulou *et al* 2018) or MR fingerprinting (Ma *et al* 2013). To improve the overall result of the SRR in future approaches, the SRR optimization scheme could be integrated in a model-based reconstruction framework as performed in Bano *et al* (2020). By that, the SRR would incorporate the acquired raw data in the entire reconstruction optimization scheme instead of using it only in the model-based T1 reconstruction as in the presented approach.

This work was only evaluated in healthy volunteers, nevertheless, from the improved visualization of pathologies in the simulated data, it can be concluded that SRR might lead to an improved image quality in patients as well.

Conclusion

In this study, a novel motion-corrected cardiac model-based SRR approach was presented, providing 3D HR T1 maps in six to ten 17 s BH. The proposed approach was successfully applied in four healthy volunteers leading to improved visualization of small structures and precise T1 values. In future studies, an integration of the BH alignment and the T1 reconstruction into the optimization scheme could further improve the results.

Acknowledgments

The authors gratefully acknowledge funding from the German Research Foundation (GRK2260, BIOQIC).

The results presented here have been developed in the framework of the 18HLT05 QUIERO Project. This project has received funding from the EMPIR programme co-financed by the Participating States and from the European Union's Horizon 2020 research and innovation programme.

Ethical statement

The research was approved by the institution's ethical committee ('Ethikkommission der PTB'). The research was conducted in accordance with the principles embodied in the Declaration of Helsinki and in accordance with local statutory requirements. All subjects gave written informed consent before participation. No approval ID number was specified.

ORCID iDs

Simone Hufnagel  <https://orcid.org/0000-0003-3942-5113>

Selma Metzner  <https://orcid.org/0000-0001-8879-1895>

Kirsten Miriam Kerkering  <https://orcid.org/0000-0002-8165-5943>

Christoph Stefan Aigner  <https://orcid.org/0000-0003-3618-9610>

Andreas Kofler  <https://orcid.org/0000-0001-9169-2572>

Jeanette Schulz-Menger  <https://orcid.org/0000-0003-3100-1092>

Tobias Schaeffter  <https://orcid.org/0000-0003-1310-2631>

Christoph Kolbitsch  <https://orcid.org/0000-0002-4355-8368>

References

- Al-Wakeel-Marquard N et al 2021 Diffuse myocardial fibrosis by T1 mapping is associated with heart failure in pediatric primary dilated cardiomyopathy *Int. J. Cardiol.* **333** 219–25
- Bano W et al 2020 Model-based super-resolution reconstruction of T2 maps *Magn. Reson. Med.* **83** 906–19
- Basty N and Grau V 2018 Super resolution of cardiac cine MRI Sequences using deep learning *Lecture Notes in Computer Science (Including Subseries Lecture Notes in Artificial Intelligence and Lecture Notes in Bioinformatics)* (Springer International Publishing) vol 11040 LNCS, 23–31
- Becker K M et al 2020 Fast myocardial T1 mapping using cardiac motion correction *Magn. Reson. Med.* **83** 438–51
- Becker K M, Schulz-Menger J, Schaeffter T and Kolbitsch C 2019 Simultaneous high-resolution cardiac T1 mapping and cine imaging using model-based iterative image reconstruction *Magn. Reson. Med.* **81** 1080–91
- Beirinx Q et al 2022 Model-based super-resolution reconstruction with joint motion estimation for improved quantitative MRI parameter mapping *Comput. Med. Imaging Graph.* **100** 102071
- Beirinx Q et al 2020 Joint maximum likelihood estimation of motion and T1 parameters from magnetic resonance images in a super-resolution framework: a simulation study ed S Brunetti et al *Fundam. Inform.* **172** 105–28
- Bhatia K K, Price A N, Shi W, Hajnal J V and Rueckert D 2014 Super-resolution reconstruction of cardiac MRI using coupled dictionary learning *2014 IEEE 11th Int. Symp. on Biomedical Imaging (ISBI)* (Piscataway, NJ: IEEE) pp 947–50
- Block K T, Uecker M and Frahm J 2007 Undersampled radial MRI with multiple coils. Iterative image reconstruction using a total variation constraint *Magn. Reson. Med.* **57** 1086–98
- Captur G et al 2016 A medical device-grade T1 and ECV phantom for global T1 mapping quality assurance—the T1 mapping and ECV standardization in cardiovascular magnetic resonance (TIMES) program *J. Cardiovasc. Magn. Reson.* **18** 1–20 Published online
- Chambolle A 2004 An algorithm for total variation minimization and applications *J. Math. Imaging Vis.* **20** 89–97
- Christodoulou A G et al 2018 Magnetic resonance multitasking for motion-resolved quantitative cardiovascular imaging *Nat. Biomed. Eng.* **2** 215–26
- Corona V, Aviles-Rivero A, Debroux N, Le Guyader C and Schönlieb C B 2021 Variational multi-task MRI reconstruction: Joint reconstruction, registration and super-resolution *Med. Image Anal.* **68** 101941
- Cruz G et al 2020 3D free-breathing cardiac magnetic resonance fingerprinting *NMR Biomed.* **33** 1–16
- de Senneville B D et al 2020 Optimizing 4D abdominal MRI: image denoising using an iterative back-projection approach *Phys. Med. Biol.* **65** 015003
- Dzyubachyk O et al 2013 Improved myocardial scar characterization by super-resolution reconstruction in late gadolinium enhanced MRI *Medical Image Computing and Computer-Assisted Intervention – MICCAI 2013* (Berlin: Springer) pp 147–54
- Dzyubachyk O et al 2015 Super-resolution reconstruction of late gadolinium-enhanced MRI for improved myocardial scar assessment *J. Magn. Reson. Imaging* **42** 160–7
- Ebner M et al 2020 An automated framework for localization, segmentation and super-resolution reconstruction of fetal brain MRI *Neuroimage* **206** 116324
- Etienne A, Botnar R M, van Muiswinkel A M C, Boesiger P, Manning W J and Stuber M 2002 Soap-Bubble? visualization and quantitative analysis of 3D coronary magnetic resonance angiograms *Magn. Reson. Med.* **48** 658–66
- Ferreira da Silva T et al 2020 Single breath-hold saturation recovery 3D cardiac T1 mapping via compressed SENSE at 3T *Magn. Reson. Mater. Phys. Biol. Med.* **33** 865–76
- Gholipour A, Estroff J A and Warfield S K 2010 Robust super-resolution volume reconstruction from slice acquisitions: application to fetal brain MRI *IEEE Trans. Med. Imaging* **29** 1739–58
- Giri S et al 2009 T2 quantification for improved detection of myocardial edema *J. Cardiovasc. Magn. Reson.* **11** 56
- Greenspan H, Oz G, Kiryati N and Peled S 2002 MRI inter-slice reconstruction using super-resolution *Magn. Reson. Imaging* **20** 437–46
- Guo R et al 2022 Emerging techniques in cardiac magnetic resonance imaging *J. Magn. Reson. Imaging* **55** 1043–59
- Guo R, Chen Z, Wang Y, Herzka D A, Luo J and Ding H 2018 Three-dimensional free breathing whole heart cardiovascular magnetic resonance T1 mapping at 3 T *J. Cardiovasc. Magn. Reson.* **20** 64
- Haaf P, Garg P, Messroghli D R, Broadbent D A, Greenwood J P and Plein S 2016 Cardiac T1 mapping and extracellular volume (ECV) in clinical practice: a comprehensive review *J. Cardiovasc. Magn. Reson.* **18** 89
- Han P K et al 2022 Free-breathing 3D cardiac T1 mapping with transmit B1 correction at 3T *Magn. Reson. Med.* **87** 1832–45
- Huang L et al 2020 FAST single-breathhold 2D multislice myocardial T1 mapping (FAST1) at 1.5T for full left ventricular coverage in three breathholds *J. Magn. Reson. Imaging* **51** 492–504
- Kainz B et al 2015 Fast volume reconstruction from motion corrupted stacks of 2D slices *IEEE Trans. Med. Imaging* **34** 1901–13
- Keith G A, Rodgers C T, Chappell M A and Robson M D 2017 A look-locker acquisition scheme for quantitative myocardial perfusion imaging with FAIR arterial spin labeling in humans at 3 tesla *Magn. Reson. Med.* **78** 541–9
- Kuklisova-Murgasova M, Quaghebeur G, Rutherford M A, Hajnal J V and Schnabel J A 2012 Reconstruction of fetal brain MRI with intensity matching and complete outlier removal *Med. Image Anal.* **16** 1550–64
- Liu D C and Nocedal J 1989 On the limited memory BFGS method for large scale optimization *Math. Program.* **45** 503–28
- Ludwig J, Speier P, Seifert F, Schaeffter T and Kolbitsch C 2021 Pilot tone-based motion correction for prospective respiratory compensated cardiac cine MRI *Magn. Reson. Med.* **85** 2403–16
- Ma D et al 2013 Magnetic resonance fingerprinting *Nature* **495** 187–92
- Mao X et al 2022 Simultaneous multi-slice cardiac MRI multitasking for motion-resolved, non-ECG, free-breathing T1–T2 mapping *Front Cardiovasc. Med.* **9** 1–13
- McDonagh S et al 2017 Context-sensitive super-resolution for fast fetal magnetic resonance imaging *Lecture Notes in Computer Science (Including Subseries Lecture Notes in Artificial Intelligence and Lecture Notes in Bioinformatics)* vol 10555, pp 116–26 LNCS

- Milotta G, Bustin A, Jaubert O, Neji R, Prieto C and Botnar R M 2020 3D whole-heart isotropic-resolution motion-compensated joint T1/T2 mapping and water/fat imaging *Magn. Reson. Med.* **84** 3009–26
- Nordio G et al 2020 Faster 3D saturation-recovery based myocardial T1 mapping using a reduced number of saturation points and denoising *PLoS One* **15** e0221071
- Nordio G, Henningsson M, Chiribiri A, Villa A D M, Schneider T and Botnar R M 2017 3D myocardial T1 mapping using saturation recovery *J. Magn. Reson. Imaging* **46** 218–27
- Odille F, Bustin A, Chen B, Vuissoz P A and Felblinger J 2015 Motion-corrected, super-resolution reconstruction for high-resolution 3D cardiac cine MRI *Lecture Notes in Computer Science (Including Subseries Lecture Notes in Artificial Intelligence and Lecture Notes in Bioinformatics)* vol 9351, pp 435–42
- Padfield D 2012 Masked object registration in the fourier domain *IEEE Trans. Image Process.* **21** 2706–18
- Pauly J, Le Roux P, Nishimura D and Macovski A 1991 Parameter relations for the Shinnar-Le Roux selective excitation pulse design algorithm (NMR imaging) *IEEE Trans. Med. Imaging* **10** 53–65
- Plenge E et al 2012 Super-resolution methods in MRI: can they improve the trade-off between resolution, signal-to-noise ratio, and acquisition time? *Magn. Reson. Med.* **68** 1983–93
- Qi H et al 2019 Free-running 3D whole heart myocardial T1 mapping with isotropic spatial resolution *Magn. Reson. Med.* **82** 1331–42
- Qi H et al 2020 Respiratory motion-compensated high-resolution 3D whole-heart T1 ρ mapping *J. Cardiovasc. Magn. Reson.* **22** 12
- Rahman S u and Wesarg S 2010b Combining short-axis and long-axis cardiac MR images by applying a super-resolution reconstruction algorithm *Med. Imaging 2010: Image Process.* **7623** 762301
- Rahman S U R and Wesarg S 2010a Upsampling of cardiac MR images: comparison of averaging and super-resolution for the combination of multiple views *Proc. of the 10th IEEE Int. Conf. on Information Technology and Applications in Biomedicine* vol 10 (Piscataway, NJ: IEEE) pp 1–4
- Rueckert D, Sonoda L I, Hayes C, Hill D L G, Leach M O and Hawkes D J 1999 Nonrigid registration using free-form deformations: application to breast MR images *IEEE Trans. Med. Imaging* **18** 712–21
- Rund A, Aigner C S, Kunisch K and Stollberger R 2018 Simultaneous multislice refocusing via time optimal control *Magn. Reson. Med.* **80** 1416–28
- Schelbert E B and Messroghli D 2016 State of the art: clinical applications of cardiac T1 mapping *Radiology* **278** 658–76
- Scott A D, Keegan J and Firmin D N 2009 Motion in cardiovascular MR imaging *Radiology* **250** 331–51
- Segars W P, Sturgeon G, Mendonca S, Grimes J and Tsui B M W 2010 4D XCAT phantom for multimodality imaging research *Med. Phys.* **37** 4902–15
- Shi W et al 2013 Cardiac image super-resolution with global correspondence using multi-atlas patchmatch *Lecture Notes in Computer Science (Including Subseries Lecture Notes in Artificial Intelligence and Lecture Notes in Bioinformatics)* vol 8151, pp 9–16
- Shilling R Z, Robbie T Q, Bailloeuil T, Mewes K, Mersereau R M and Brummer M E 2009 A super-resolution framework for 3D high-resolution and high-contrast imaging using 2D multislice MRI *IEEE Trans. Med. Imaging* **28** 633–44
- Shuzhou J, Hui X, Glover A, Rutherford M and Hajnal J V 2006 A novel approach to accurate 3D high resolution and high SNR fetal brain imaging *3rd IEEE Int. Symp. on Biomedical Imaging: Macro to Nano* vol 2006 (IEEE) pp 662–5
- Sui Y, Afacan O, Gholipour A and Warfield S K 2021 Fast and high-resolution neonatal brain mri through super-resolution reconstruction from acquisitions with variable slice selection direction *Front. Neurosci.* **15** 1–15
- Sui Y, Afacan O, Gholipour A, Warfield S K and Isotropic M R I 2019 Super-resolution reconstruction with multi-scale gradient field prior *Physiology & Behavior* ed D Shen et al (Berlin: Springer) (Lecture Notes in Computer Science) 11766, pp 3–11
- Van Reeth E, Tham I W K, Tan C H and Poh C L 2012 Super-resolution in magnetic resonance imaging: a review *Concepts Magn. Reson. A* **40A** 306–25
- Van Steenkiste G et al 2017 Super-resolution T1 estimation: quantitative high resolution T1 mapping from a set of low resolution T1-weighted images with different slice orientations *Magn. Reson. Med.* **77** 1818–30
- Velasco C et al 2022 Simultaneous T1, T2, and T1 ρ cardiac magnetic resonance fingerprinting for contrast agent-free myocardial tissue characterization *Magn. Reson. Med.* **87** 1992–2002
- von Knobelsdorff-Brenkenhoff F et al 2013 Myocardial T1 and T2 mapping at 3T: reference values, influencing factors and implications *J. Cardiovasc. Magn. Reson.* **15** 53
- Wang Y, Yang J, Yin W and Zhang Y 2008 A new alternating minimization algorithm for total variation image reconstruction *SIAM J. Imaging Sci.* **1** 248–72
- Weissman N J et al 2002 Standardized myocardial segmentation and nomenclature for tomographic imaging of the heart *Circulation* **105** 539–42
- Xia Y, Ravikumar N, Greenwood J P, Neubauer S, Petersen S E and Frangi A F 2021 Super-resolution of cardiac Mr cine imaging using conditional GANs and unsupervised transfer learning *Med. Image Anal.* **71** 102037